

SUBMITTED FOR PUBLICATION TO: DR. D. JOSEPH, UNIVERSITY OF ALBERTA, SEPTEMBER 24, 2007

Simulation of Photodetectors in Hybrid Image Sensors

Dan Sirbu

Simulation of Photodetectors in Hybrid Image Sensors

Abstract

Hybrid image sensors combine advantages of the two leading imaging technologies (the fill factor of CCD, and the signal processing of CMOS) via vertical integration. This report derives a simple model for the photodetector of the hybrid image sensor, and the affiliated set of differential equations. This bounded-value problem is subsequently solved numerically in 1D, and a simple analytical model is derived from the numerical solution. Lastly, simulation results are presented, including an optimum photodetector length for best current signal level.

Index Terms

Hybrid image sensors, photodetectors, vertical integration, numerical solution, analytical model.

I. INTRODUCTION

The advent of the pinhole camera permitted for the first time the capture of images; the evolution of more complex film cameras in the 19th and 20th centuries revolutionized the way in which visual information was captured, disseminated, and understood. In recent decades, the prevalence of digital cameras has initiated a second revolution in terms of accessibility to visual information.

The two currently prevailing digital imaging technologies on the market are the charge-coupled device (CCD) and the complementary metal-oxide-semiconductor (CMOS). Although they each present their individual strengths and weaknesses, strong interest from manufacturers from across the divide has led to a strong convergence of performance characteristics. For instance, while CMOS sensors were initially touted for the low-cost, low-

quality market, in recent years they have been adopted in high-performance digital SLRs (most prominently, in Canon's product offering). Over the past decade, CMOS technology has made inroads in the CCD-dominated digital camera market to the point that parity has been achieved between these two rival technologies [1].

Vertical integration holds the promise of combining the strengths of both CCD and CMOS sensors in one device. Hybrid image sensors are one type of vertically-integrated device; in this report photodetectors of such hybrid image sensors are simulated for the purpose of optimizing the photodetector length for best current signal reception.

II. CCD vs. CMOS

The CCD is essentially an analog shift register wherein charge is transferred through successive capacitive stages. The CCD (as shown in Fig. 1) consists of an array of pixels, whose individual area is mostly photosensitive to the incident light. Excess charge carriers formed in the semiconductive layer accumulate in potential wells for each individual pixel. Charge is transferred repeatedly across the rows by the simultaneous emptying of potential wells, and then across the columns to an output amplifier. The main advantage of CCD detectors is that the area available for photodetectors (referred to as fill factor) is maximized, thus allowing for the capture of more light photons (increased quantum efficiency), and a better image quality due to the higher resolution and sensitivity. CCD photodetectors were quickly adopted by the astronomical community to replace photographic films especially because of the very good sensitivity characteristics associated from a larger fill factor. With a four-decade old market presence, fabrication processes for CCD photodetectors are optimised for image quality (high SNR), efficient charge transfer, accurate detector geometry, and minimized parasitic dark current. Conversely, the disadvantage is that CMOS circuitry for signal processing is not easily integrated with the CCD detector, often being added externally.

This added level of complexity increases fabrication costs of CCD technology and delays the conversion from analogue to digital signal. The CCD detector itself is susceptible to damage due to the successive stage nature of signal retrieval, which means that the loss of an individual stage results in the loss of an entire column.

[Fig. 1 about here.]

The CMOS chip is, by contrast, an active pixel sensor. A CMOS detector is arranged as a memory array of pixel cells, with each individual pixel addressable by row and column as depicted in Fig. 2. Incident light strikes the photodetector, which also creates excess charge carriers that produce a signal. Extra circuitry is placed next to the photodetector for signal detection, and the conversion from analogue to digital signal format. The advantage of CMOS detectors is that they can potentially use fewer components and are inherently less susceptible to analogue noise due to the integration of on-pixel signal processing. Furthermore, CMOS pixels are individually addressable eliminating the difficulties associated with successive charge transfer. CMOS technology can be manufactured more cheaply in CMOS foundries, use less power, and have faster integration times, but may result in lower quality images and needing more advanced calibration techniques [1].

[Fig. 2 about here.]

III. VERTICAL INTEGRATION EMERGING TECHNOLOGIES

A spate of technologies has emerged in recent years that seek to combine the benefits of both CCD and CMOS in a more compact package. A technique to achieve this end is via vertical integration, the capture of incident light on the photodetector on a top level and ASIC signal processing circuitry on a lower level. This achieves the high fill-factor prevalent in CCD and also the near placement of circuitry relative to the individual pixel as in CMOS.

This paradigm mimics the human eye, which also features a top layer of photodetectors (the retina) and signal processing in subsequent levels.

A. *Thin Film on ASIC*

The structure of a thin film on ASIC (TFA) photodetector can be seen in Fig. 3. Light enters through a transparent substrate, and a subsequent transparent conductive oxide (TCO) layer permits light passage; amorphous hydrogenated silicon (a-Si:H) acts as the photosensitive film. Excess charge carriers generate a current signal that is received at the aluminum contacts, and then further to the CMOS readout circuitry (located in the ASIC layer in the substrate below a separating insulation). The advantages of TFA are that fill factor is maximized, that the photodetector material properties can be changed for different light reception, and that signal processing is done close to the photodetector. However, the thin film must be grown on the ASIC in a multi-step process, which can make fabrication expensive and susceptible to parameter changes when exposed to heat during a subsequent fabrication step. Lateral current between adjacent photodetectors contributes to image smearing to the extent that it may be necessary to grow insulation barriers between adjacent photodetectors and/or use regulatory circuitry for maintaining a level potential at the aluminum contacts [2].

[Fig. 3 about here.]

B. *Silicon-On-Insulator*

The silicon-on-insulator (SOI) photodetector receives light via a conductive substrate; an epitaxial crystalline silicon layer is excited by light to produce excess carrier charges and a corresponding current signal [3]. The signal processing circuitry is embedded in silicon device layer, separated by an insulating layer. This structure can be observed in (refer to

Fig. 4).

[Fig. 4 about here.]

C. Flip Chip

Flip-chip structure is similar to the TFA, but rather than growing the thin film on top of the ASIC layer, a hybrid technique is utilized. The film is grown separately and then flipped on top of the IC layer, bonded on metallic contacts. This hybrid technology is more conducive to fabrication than TFA, having the benefit of eliminating the multi-stage growing process. It is theoretically more difficult to obtain a small pitch due to alignment requirements, although in actual practice TFA detectors exhibit larger pitch size. The structure of the flip-chip is shown in Fig. 5.

The hybrid image sensor technology is preferred for investigation of vertical integration because of its relative ease of fabrication whilst maintaining good performance characteristics.

[Fig. 5 about here.]

IV. PROBLEM STATEMENT

The drift-diffusion differential equations are studied in a one-dimensional hybrid photodetector with the goal of determining a photodetector length l_{opt} that optimizes the contrast ratio of signal current density J_{ph} (due to optical generation from the incoming photon flux) to background current density J_{dk} (a dark, parasitic effect) for best imaging quality. Light enters the photodetector and excites the Fermi energy levels of the semiconductive amorphous hydrogenated Silicon to generate excess holes δp and excess electrons δn (always in electron-hole pairs), with an exponentially attenuated optical generation profile across the photodetector length. Drift current is associated with the difference in potential between the two terminals of the photodetector, whereas diffusion current is due to difference

in the concentration of the excess carrier charges generated by light excitation across the photodetector.

This represents a bounded-value coupled set of nonlinear differential equations. A numerical solution is sought to determine the distribution of the potential and the excess charge carriers across the photodetectors. The design goal of this simulation is to determine an optimal length for which the contrast ratio β is maximal, with contrast defined by:

$$\beta = \frac{J_{ph}}{J_{dk}} \quad (1)$$

V. PHOTODETECTOR MODEL

The photodetector model is simplified to take into account only the variation in flux across the length of the photodetector (a 1D model) as based on the optical attenuation of the material. This model is abstracted to a two-terminal device with three different regions Fig. 6. A potential difference V_{AB} is applied across the two terminals. A central semiconductor of length l represents the photodetector itself, with two resistive regions at either end of the semiconductor of conductivities σ_A and σ_B and lengths l_A and l_B respectively. Essentially, the effect of the added interface resistances is to change the potential at the boundaries of the semiconductor region due to the potential drop across the resistor region. This ensures that there exists an optimum length.

[Fig. 6 about here.]

With the existence of excess charge carriers, free charge is present in the photodetector, which implies that the internal potential distribution V_{int} must satisfy Poisson's equation:

$$\frac{d^2 V_{int}}{dz^2} = -\frac{q}{\epsilon}(\delta p(z) - \delta n(z)) \quad (2)$$

The continuity equations are derived from two Maxwell equations (Ampère's law and Gauss' Law) and model the conservation law for free charge:

$$r(z) - g(z) = -\frac{1}{q} \frac{dJ_p(z)}{dz} = \frac{1}{q} \frac{dJ_n(z)}{dz} \quad (3)$$

Where $r(z)$ and $g(z)$ are the rates of electron-hole pair recombination and electron-hole pair generation respectively. J_p and J_n are the hole and electron current densities, which are given by drift-diffusion. For the hole current-density:

$$J_p(z) = q\mu_p p(z)E(z) - qD_p \frac{d}{dz} p(z) \quad (4)$$

And for the electron current-density:

$$J_n(z) = q\mu_n n(z)E(z) + qD_n \frac{d}{dz} n(z) \quad (5)$$

Using a simple, direct-recombination model:

$$r(z) = \alpha_r p(z)n(z) \quad (6)$$

and optical generation is attenuated exponentially with length across the photodetector, giving the ensuing generation function when thermal generation g_{th} is also considered:

$$g(z) = \underbrace{\alpha_r n_i^2}_{g_{th}} + \underbrace{\eta \alpha \phi_0 (1 - R) e^{-\alpha z}}_{g_{op}} \quad (7)$$

The electric field is, by definition, the gradient of the potential distribution:

$$E(z) = -\frac{d}{dz} V(z) \quad (8)$$

The positive charge carrier concentration $p(z)$ is defined in terms of the deviation $\delta p(z)$ from the nominal concentration p_0 :

$$p(z) = p_0 + \delta p(z) \quad (9)$$

Likewise, for the negative charge carrier $n(z)$ is defined in terms of the deviation $\delta n(z)$ from the nominal concentration n_0 :

$$n(z) = n_0 + \delta n(z) \quad (10)$$

To solve this boundary value problem, the basic equations must be augmented by a set of boundary conditions. For the Poisson equation in (2):

$$V_{int}(0) = V_{int}(l) = 0 \quad (11)$$

For the continuity system in (3), two boundary conditions are needed. As no external recombination is assumed in the model thus far described, this implies that generation and recombination must be in balance:

$$\int_0^l r(z) - g(z) dz = 0 \quad (12)$$

The fact that these boundary conditions are sufficient and necessary shall be demonstrated from a numerical standpoint using singular value decomposition.

VI. NUMERICAL TECHNIQUES

A. Backslash Operator

The Matlab backslash operator \backslash is used for efficiently solving linear equations of the form:

$$\mathbf{Ax} = \mathbf{b} \quad (13)$$

Provided that matrix \mathbf{A} is not rank-deficient, the backslash operator solution uses an automatic solver that selects the most efficient numerical technique for determining the equation roots based upon the form of \mathbf{A} (sparse, banded, regular) [4]. If an exact solution cannot

be found, a least-squares solution will be attempted instead; it is thus important the exact number of boundary conditions be used to augment the rank-deficient coefficient matrix, or risk introducing error into the solution. The backslash solution is as follows:

$$\mathbf{x} = \mathbf{A} \backslash \mathbf{b} \quad (14)$$

B. Singular Value Decomposition

Singular Value Decomposition (SVD) is a factorization technique that diagonalizes arbitrary-sized matrices on the basis of eigenvectors [5]. For a matrix \mathbf{A} of arbitrary $m \times n$ size, the SVD is given by:

$$\mathbf{A} = \mathbf{U} \mathbf{S} \mathbf{V}^* \quad (15)$$

In the above SVD, \mathbf{U} is a unitary square matrix of dimension m , \mathbf{S} is $m \times n$ with non-negative entries only on the diagonals, and \mathbf{V}^* is a transpose of \mathbf{V} , a unitary matrix over the field K from which the entries of \mathbf{A} are derived. The matrix \mathbf{S} contains across its diagonals the singular values of matrix \mathbf{A} . Thus the rank of \mathbf{A} can be derived from the number of non-zero entries in the diagonal of \mathbf{S} . This is useful in determining if the matrix \mathbf{A} needs to be augmented by a set of boundary conditions before solving with the backslash operator, and if the proposed boundary conditions are independent (i.e., not linear combinations of equations already implied by \mathbf{A}).

C. Matrix Ill-Conditioning

An ill-conditioned system occurs when, although the coefficient matrix is not singular, one or more of the singular values are orders of magnitude less than the rest (i.e., it is close to being singular). The condition number for the linear equation in (13) gives a measure of

how accurate digital computation of the system will be:

$$\text{Cond}[\mathbf{A}] = \|\mathbf{A}\| \|\mathbf{A}^{-1}\| \quad (16)$$

D. Fixed-Point Iteration

Fixed-point iteration, sometimes also called successive substitution, is an open method for determining the root of an equation [4]. In contrast to a bracketed method, fixed-point iteration only requires one initial guess for the root but there is no guarantee of convergence to the root. The general fixed-point equation is:

$$x_{i+1} = y(x_i) \quad (17)$$

E. Convergence Tracking

Since the fixed-point iteration method does not guarantee convergence, it is necessary to ensure that a method of tracking the convergence of the root is incorporated in the solution. One such method is to specify a level of approximate error tolerance ϵ_T and interrupt the iterative process when the tolerance limit has been attained between successive iterations (i.e., $\epsilon_A < \epsilon_T$):

$$\epsilon_A = \frac{\|x_{i+1} - x_i\|}{\|x_{i+1}\|} \times 100\% \quad (18)$$

A maximum number of iterations is specified to avoid an infinite iterative loop in the case when the method is not converging.

F. Addition of Small Numbers

When adding or subtracting numbers orders of magnitude apart, information about the smaller number can be minimized and even lost if the order difference approaches the machine-precision (eps) limit [4]. In the problem at hand, small deviations from the average

carrier concentration hold important information regarding the internal field distribution and charge continuity. Thus, for a robust numerical solution it would be necessary to state the set of equations so that addition of highly dissimilar numbers is avoided.

G. Elementwise Multiplication

A novel operator \circ is defined for linear algebra manipulation that mirrors the element-by-element multiplication oftentimes used by computer programmers, as suggested by [1]. The advantage of this operator, as will be shown later, is that it permits the factoring of certain terms thus avoiding the problems associated with addition of dissimilar numbers. Drawing parallels to multilinear algebra the \circ operator functions as follows:

$$c_i = a_{\underline{i}}b_{\underline{i}} \Leftrightarrow \mathbf{c} = \mathbf{a} \circ \mathbf{b} \quad (19)$$

$$c_{ij} = a_{\underline{ij}}b_{\underline{ij}} \Leftrightarrow \mathbf{C} = \mathbf{A} \circ \mathbf{B} \quad (20)$$

$$c_{ij} = a_{\underline{ij}}b_{\underline{i}} \Leftrightarrow \mathbf{C} = \mathbf{A} \circ \mathbf{b} \quad (21)$$

H. Finite Differences vs. Finite Element

To numerically solve for the differential equations described previously, a discrete approximation of the derivative is required. Finite differences are used to discretize the photodetector length domain z for both the Poisson equation and for the continuity system (thus, a 1D finite-difference scheme); divided finite differences represent the actual discrete approximation of the derivative, with the resulting difference equations between the nodes being the analogue of the differential equation. Solving the difference equations yields the sought values at the nodes. The finite difference method works best for cases when the domain is regularly-shaped and a rectangular-like grid can be applied easily to obtain the nodes.

A very popular method to solve boundary value problems is via the finite element

method. The first step is to rewrite the boundary value problem in a weak, variational form; the domain is then discretized by the application of a mesh, resulting in an assembly of finite elements whereby nodal values are to be determined. Interpolation functions can be applied across the element to give better approximations for points lying along the element rather than being a node point. A global system of equations is then constructed based on the connectivities between local elements, and subsequently solved to obtain solutions for node-points. The finite element method is well-suited for more complex-shapes. A contrast of the two methods is provided by [6].

In this particular problem, the finite difference method is preferred due to the regular nature of the domain. The finite difference method is also simpler to implement, and for regular domains such as these typically performs faster and with smaller error. Matlab's built-in BVP4 algorithm for solving boundary value problems employs finite element analysis, and it fails to converge to a solution for this set of equations.

VII. NUMERICAL SOLUTION

Using the three-region one-dimensional photodetector model as shown in Fig. 6, the applied voltage V_{AB} across the terminals can then be described as:

$$V_{AB} = E_A l_A + \int_0^l E(z) dz + E_B l_B \quad (22)$$

The electric field across the photodetector $E(z)$ is the summation of the component due to the applied voltage (E_{ext}) and due to the excess charge carriers generated in the photodetector ($E_{int}(z)$):

$$E(z) = E_{ext} + E_{int}(z) \quad (23)$$

Where the external electric field is defined such that:

$$E_{ext} = \frac{1}{l} \int_0^l E(z) dz \quad (24)$$

And, for the internal electric field:

$$\frac{1}{l} \int_0^l E_{int}(z) dz = 0 \quad (25)$$

Also the electric field across the contact resistors can be written in terms of current density J as:

$$E_A = \frac{J}{\sigma_A}, \quad E_B = \frac{J}{\sigma_B}, \text{ where: } J = \frac{1}{l} \int_0^l (J_p(z) + J_n(z)) dz \quad (26)$$

and defining sheet resistances for the two contact resistors in the following manner:

$$R'_A = \frac{l_a}{\sigma_a}, \quad R'_B = \frac{l_B}{\sigma_B}, \quad R'_C = R'_A + R'_B \quad (27)$$

So that (23) can now be written more simply as:

$$V_{AB} = JR'_C + E_{ext}l \quad (28)$$

Mean quantities are defined using the overline (e.g., for the mean hole concentration \bar{p}):

$$\bar{p} = \frac{1}{l} \int_0^l p(z) dz \quad (29)$$

For the sake of numerical robustness, charge concentrations are defined in terms of deviation from mean excess charge concentration values:

$$p(z) = p_0 + \delta p(z) = \bar{p} + \gamma_p(z), \text{ where: } \bar{p} = \frac{1}{l} \int_0^l p(z) dz, \quad \int_0^l \gamma_p(z) dz = 0 \quad (30)$$

$$n(z) = n_0 + \delta n(z) = \bar{n} + \gamma_n(z), \text{ where: } \bar{n} = \frac{1}{l} \int_0^l n(z) dz, \quad \int_0^l \gamma_n(z) dz = 0 \quad (31)$$

Letting conductivity σ be:

$$\sigma(z) = q(\mu_p p(z) + \mu_n n(z)), \text{ then: } \sigma_{dk} = q(\mu_p p_0 + \mu_n n_0), \quad \sigma_{ph} = q(\mu_p \bar{\delta p} + \mu_n \bar{\delta n}) \quad (32)$$

Thus, current density can be written as a composition due to externally applied voltage and internally from excess charge:

$$J(z) = J_{ext} + J_{int}(z) = \frac{(\sigma_{dk} + \sigma_{ph})V_{AB} + lJ_{int}(z)}{l + (\sigma_{dk} + \sigma_{ph})R'_c} \quad (33)$$

where:

$$J_{ext} = \bar{\sigma}E_{ext}, \quad J_{int}(z) = \frac{q}{l} \int_0^l (\mu_p \gamma_p(z) + \mu_n \gamma_n(z))(E_{int}(z) - D_p \frac{d\gamma_p(z)}{dz} + D_n \frac{d\gamma_n(z)}{dz}) dz \quad (34)$$

Boundary conditions must be used to augment the continuity system. From charge neutrality:

$$\frac{1}{l} \int_0^l (\delta p(z) - \delta n(z)) dz = 0 \Rightarrow \bar{\delta p} = \bar{\delta n} \quad (35)$$

and the value for $\bar{\delta n}$ from the recombination/generation charge balance condition:

$$\frac{1}{l} \int_0^l (r(z) - g(z)) dz = 0 \quad (36)$$

substituting for the direct recombination from (6) and generation from (7):

$$\frac{1}{l} \int_0^l (\alpha_r (\bar{p} + \gamma_p)(\bar{n} + \gamma_n) - (\eta \phi_0 (1 - R) e^{-\alpha z} + \alpha_r n_0 p_0)) dz = 0 \quad (37)$$

After simplification, the mean excess charge carrier concentration $\bar{\delta n}$ is given by the quadratic:

$$\alpha_r \bar{\delta n}^2 + \alpha_r (p_0 + n_0) \bar{\delta n} - \frac{\eta \phi_0 (1 - R) (1 - e^{-\alpha l})}{l} + \frac{\alpha_r}{l} \int_0^l (\gamma_p(z) \circ \gamma_n(z)) dz = 0 \quad (38)$$

The Poisson equation in terms of deviation quantities:

$$\frac{d^2 V}{dz^2} = \frac{q}{\epsilon} (\gamma_p - \gamma_n) \quad (39)$$

The boundary condition being the definition of E_{int} from (25).

Thus, given the deviation quantities γ_p and γ_n , all other quantities of interest, namely $E_{int}(z)$, E_{ext} , $\overline{\delta n}$, $\overline{\delta p}$, J_{ext} , $J_{int}(z)$ are all deducible. Thus, given an initial guess for γ_p and γ_n and using a fixed-point iteration process, the continuity system & Poisson can be used to update all of these quantities.

Defining matrix D as a differentiation matrix and rewriting the set of differential equations using the \circ operator:

$$r - g = \alpha_r p_0 \delta \mathbf{n} + \alpha_r n_0 \delta \mathbf{p} + \alpha_r \delta \mathbf{p} \circ \delta \mathbf{n} - \mathbf{g}_{op} \quad (40)$$

$$-\frac{1}{q} \mathbf{D} \mathbf{J}_p = \mu_p p_0 \mathbf{D}^2 \mathbf{V} + \mathbf{D}(\mu_p \mathbf{I} \circ \mathbf{D} \mathbf{V} + D_p \mathbf{D}) \delta \mathbf{p} \quad (41)$$

$$\frac{1}{q} \mathbf{D} \mathbf{J}_n = \mu_n n_0 \mathbf{D}^2 \mathbf{V} - \mathbf{D}(\mu_n \mathbf{I} \circ \mathbf{D} \mathbf{V} + D_n \mathbf{D}) \delta \mathbf{n} \quad (42)$$

From (40) and (41), in terms of deviation quantities:

$$\gamma_p \left(\alpha_r n_0 \mathbf{I} + \mu_p \left(\mathbf{I} \circ \left(\mathbf{D} \mathbf{E} + \frac{p_0 q}{\epsilon} \right) + \mathbf{I} \circ \mathbf{E} \right) - D_p \mathbf{D}^2 \right) + \gamma_n \left(p_0 \alpha_r - \frac{\mu_p}{q} \right) = \quad (43)$$

$$\mathbf{g}_{op} - \alpha_r (p_0 + n_0 + \overline{\delta n}) \overline{\delta n} + \gamma_p \circ \gamma_n \quad (44)$$

Likewise from (40) and (42):

$$\gamma_p \left(\alpha_r n_0 \mathbf{I} - \frac{\mu_n q}{\epsilon} \right) + \gamma_n \left(\alpha_r p_0 \mathbf{I} - \mu_n \left(\mathbf{I} \circ \left(\mathbf{D} \mathbf{E} + \frac{n_0 q}{\epsilon} \right) + \mathbf{I} \circ \mathbf{E} \right) - D_n \mathbf{D}^2 \right) = \quad (45)$$

$$\mathbf{g}_{op} - \alpha_r (p_0 + n_0 + \overline{\delta n}) + \gamma_p \circ \gamma_n \quad (46)$$

Which system is augmented with the two extra conditions derived from the definition of the deviations γ_p and γ_n :

$$\int_0^l \gamma_p dz = 0 \quad (47)$$

$$\int_0^l \gamma_n dz = 0 \quad (48)$$

And lastly, the Poisson equation from (39) in terms of deviation vectors and differentiation matrix D :

$$\mathbf{D}\mathbf{E}_{int} = -\frac{q}{\epsilon}(\gamma_p - \gamma_n) \quad (49)$$

Where E_{int} was substituted instead of DV . The boundary condition is now:

$$\int_0^l \mathbf{E}_{int} dz = 0 \quad (50)$$

VIII. ANALYTICAL SOLUTION

To derive an analytical solution, a reasonable approximation to make is that the deviations γ_p and γ_n are negligible compared to the mean excess carrier concentration. Thus, letting:

$$\gamma_p = \gamma_n = 0 \quad (51)$$

Which implies that the quadratic equation in (38):

$$\alpha_r \bar{\delta n}^2 + \alpha_r (p_0 + n_0) \bar{\delta n} - \frac{\eta \phi_0 (1 - R)(1 - e^{-\alpha l})}{l} = 0 \quad (52)$$

And hence, all other implied quantities follow:

$$E_{int} = J_{int} = 0, \quad E_{ext} = \frac{V_{AB}}{l + (\sigma_{dk} + \sigma_{ph})R'_c}, \quad J = J_{ext} = \frac{(\sigma_{dk} + \sigma_{ph})V_{AB}}{l + (\sigma_{dk} + \sigma_{ph})R'_c} \quad (53)$$

In the dark case (i.e., $\phi = 0$), it follows that:

$$\bar{\delta n} = \sigma_{ph} = E_{int} = 0, \quad E_{ext} = \frac{V_{AB}}{l + \sigma_{dk}R'_c}, \quad J = J_{dk} = \frac{\sigma_{dk}V_{AB}}{l + \sigma_{dk}} \quad (54)$$

IX. NUMERICAL IMPLEMENTATION

The numerical implementation must be modularized for ease of debugging and reuse, must be extensible for addition of new materials & test case parameters, and robust for a wide region of input flux and applied voltages.

A. Solver

The flowchart in Fig. 7 captures an overview of the tasks performed by the numerical solver routine to calculate a solution given a set of initial conditions. As part of the inputs to the numerical solver routine the following must be specified: material properties, simulation parameters, convergence limits. The output consists of a structure that contains all the sought quantities.

[Fig. 7 about here.]

The solver starts with an initialization process. In this stage all fields in the solution structure are first declared; then, the light absorption profile is generated, and a number of the necessary coefficient matrices are created. In particular, for the Poisson system, the left-hand-side coefficient matrix does not depend on the iterative process so it can be created before the iteration and will maintain the same values throughout. The Poisson system is augmented using the definition of E_{int} as detailed previously in (50), while integrating vectors are generated for continuity system boundary conditions and also first and second-order differentiation matrices. Some values can be computed without the need for entering the iterative process, such as the dark current and also the dark conductivity which are entirely dependent upon the applied voltage, material properties, and simulation parameters. Initial guess values for the mean excess charge carrier concentration and for the external field are computed by solving the quadratic equation in (52) and needed as starting points for the

iterative process.

The iterative process is controlled by two input simulation parameters: a relative error tolerance and a maximum number of loops. Default values exist, should these not be specified when the solver is invoked. The iterative process essentially improves the guess of the excess charge carrier concentration by recomputing the deviations γ_p and γ_n at each iteration. This is achieved by first solving the continuity equation for the required deviations; then using these newly updated values the mean carrier charge concentration is obtained as well as values for other flux-dependent quantities such as internal current density J_{int} , the photosensitive conductivity, and the external field E_{ext} . At the end of each iteration, the convergence test is based upon the newly updated values of deviation versus the previous guess.

Upon termination of the iterative loop, the last stage is the wrapping-up computation of external field, total field, potential, carrier concentration, and current densities before returning the solution structure.

B. Numerical Differentiation

For implementing the numerical solver, it is necessary to create a differentiation matrix \mathbf{D} that when multiplied with vector \mathbf{x} of size n returns a vector b also of size n with the values of the derivative at each of the points [4]. Thus preserving the size of the original vector is one requirement but it must be done such that the degree of error is maintained constant throughout the output vector. A differentiation matrix is proposed based on the centre-difference approximation of the first derivative at all centre points, with higher-order forward- and backward-approximations at the edges that give a constant $O(h^2)$ error.

Centre differences:

$$f'(x_i) = \frac{f(x_{i+1}) - f(x_{i-1}))}{2h} + O(h^2) \quad (55)$$

Forward-differences:

$$f'(x_i) = \frac{-f(x_{i+2}) + 4f(x_{i+1}) - 3f(x_i)}{2h} + O(h^2) \quad (56)$$

Backward-differences:

$$f'(x_i) = \frac{3f(x_i) - 4f(x_{i-1}) + f(x_{i-2})}{2h} + O(h^2) \quad (57)$$

And combining all this in a coefficient-matrix form:

$$\mathbf{D} = \begin{pmatrix} -\frac{3}{2} & 2 & -\frac{1}{2} & 0 & 0 & \dots & 0 \\ 0 & -\frac{1}{2} & 0 & \frac{1}{2} & 0 & \dots & 0 \\ 0 & 0 & -\frac{1}{2} & 0 & \frac{1}{2} & \dots & 0 \\ \vdots & \vdots & \vdots & \ddots & \ddots & \ddots & \vdots \\ 0 & 0 & \dots & -\frac{1}{2} & 0 & \frac{1}{2} & 0 \\ 0 & 0 & \dots & 0 & \frac{1}{2} & -2 & \frac{3}{2} \end{pmatrix}$$

C. Numerical Integration

Performing integration across the length of the photodetector for various quantities is sometimes necessary, especially when implementing boundary conditions. For an n sized column vector \mathbf{x} , the n -sized integration row-vector \mathbf{M} will output a scalar result I :

$$\mathbf{M}\mathbf{x} = I \quad (58)$$

A simple integration vector is based upon the compound trapezoidal integration method.

The interval space is divided into n -equally spaced sections:

$$I = \int_{x_1}^{x_2} f(x)dx + \int_{x_2}^{x_3} f(x)dx + \dots + \int_{x_{n-1}}^{x_n} f(x)dx \quad (59)$$

and the trapezoidal rule is applied for each of the composite segments:

$$I = \frac{b-a}{n} \left(\frac{f(x_1)}{2} + \sum_{i=2}^{n-1} f(x_i) + \frac{f(x_n)}{2} \right) \quad (60)$$

This can be written in the n -sized row vector:

$$\text{intt} = \left(\frac{1}{2} \quad 1 \quad 1 \quad \dots \quad 1 \quad 1 \quad \frac{1}{2} \right)$$

D. Matrix Scaling

Matrix ill-conditioning can cause numerical error in digital computation. A technique to alleviate the ill-conditioning of the system is to multiply each linear equation by a scalar factor such that the coefficient matrix is normalized with a maximum entry magnitude of 1 for each row. For each row then the scaling factor is given by:

$$k_{\text{factor}} = \frac{1}{\max(\text{row})} \quad (61)$$

With each linear equation of the form:

$$(k_{\text{factor}} \times \text{row}_n(A)) \mathbf{x} = k_{\text{factor}} b_n \quad (62)$$

E. Sparsity

The coefficient matrices introduced in the solver are often mostly zeroes except across banded diagonals. The MATLAB backslash operator automatically detects sparse systems and chooses appropriate routines that take advantage of the system sparsity for faster numerical computation, so it is important to preserve matrix sparsity throughout.

Empty matrices are created as sparse using the `sparse()` command, sparse identity matrices are created with the `speye()` command, and `spdiags()` creates sparse matrices based on the nonzero diagonals.

X. RESULTS

The design goal of this investigation is to assist the design of a flip-chip detector by determining the optimal length for the point of maximum photocurrent to dark current ratio. Characterization of the robustness of the method in relation to various levels of injection, the strength of electric field applied in terms of convergence, as well as comparisons with the analytical solution. To obtain results, a pipeline is created as shown in Fig. 8

[Fig. 8 about here.]

A. Analytical vs. Numerical Solutions

The main difference between the analytical and numerical solutions lies in the computation of deviations γ_p and γ_n . In the analytical solution, the deviations are assumed to be negligible (i.e., set to 0) whilst the numerical solution is an improvement upon the analytical solution precisely because the iterative process computes actual deviation values.

In Fig. 9, the solution obtained from the numerical method is shown:

[Fig. 9 about here.]

Whilst the solution applying the analytical method is shown in Fig. 10:

[Fig. 10 about here.]

The most striking difference between the numerical and analytical methods is apparent when plotting the rate of optical generation as in Fig. 11; for the numerical case, it is clear that the continuity condition is violated as the optical generation does not match the actual optical generation profile.

[Fig. 11 about here.]

B. Optimal Length

To obtain the optimal length of the photodetector, the solver is run with a varying length parameter that ranges from $0.01 \mu m$ to $1 \mu m$; a photocurrent and dark current are extracted at each solver pass and the contrast ratio is plotted in Fig. 12. As seen, the maximum occurs at about $0.1 \mu m$, so this would be the optimum length that attains the best photocurrent signal relative to the dark, background current, and is the primary result of the investigation. The contrast ratio is low at small lengths due to the effect of the resistive contacts and also

at longer lengths due to the decrease in photoconductivity.

[Fig. 12 about here.]

C. Injection Levels

The numerical and analytical solutions are plotted alongside corresponding to a variety of injection levels as shown in Fig. 13. This ranges from $10^0 \frac{\text{photons}}{\text{cm}^2\text{s}}$ (dark case) to $10^{15} \frac{\text{photons}}{\text{cm}^2\text{s}}$ (high injection case).

[Fig. 13 about here.]

It can be seen that the numerical and analytical solutions are in accord with one another. This indicates that the analytical solution is actually quite a good approximation. For mid-injection, the convergence is very fast, requiring only about two iterations as shown in Fig. 14.

[Fig. 14 about here.]

D. Applied Voltage

A different test is to apply a varying external voltage to the two terminals of the photodetector and determine how the numerical and analytical results differ under different levels of external field as illustrated in Fig. 15. In this case, the two agree very well when the external electric field is large but there is a discrepancy at low electric field applied. The numerical technique does not actually seem to converge for low-electric field.

[Fig. 15 about here.]

XI. CONCLUSION

Hybrid image sensors provide potential for growth in the imaging science market through the combination of the benefits of the both mainstay technologies (CCD and CMOS) via

vertical integration. A brief photodetector model was outlined, and a numerical simulation was developed on the basis of this model to solve for the excess charge carrier concentration. An analytical model was derived from the numerical solution, and it was shown that although it violates the continuity condition and assumes a constant average excess charge carrier concentration, that results are matched very closely to the numerical simulation. The design goal of this investigation was to determine the optimal length at which to construct the photodetector, which, based on the proposed photodetector model, was found to be $0.1\mu\text{m}$.

ACKNOWLEDGEMENTS

I would like to thank Dil Joseph and Orit Skorka for their support, supervision, and contributions without which this project would not have been possible. I also gratefully acknowledge the funding support received from the Natural Sciences and Engineering Research Council (NSERC) via the Undergraduate Student Research Award (USRA).

REFERENCES

- [1] Dileepan Joseph, *Modelling and calibration of logarithmic CMOS image sensors*, Ph.D. thesis, University of Oxford, 2002.
- [2] Dan Sirbu, “Finite difference analysis of thin film photodetector,” Jan. 2007.
- [3] Ben Streetman and Sanjay Banerjee, *Solid State Electronic Devices*, Prentice-Hall, 2006.
- [4] Steven Chapra, *Numerical Methods for Engineers*, McGraw-Hill, 5th edition, 2006.
- [5] K.F. Riley, M.P. Hobson, and S.J. Bence, *Mathematical Methods for Physics and Engineering*, Cambridge University Press, 2006.
- [6] John J. Barnes and Ronald J. Lomax, “Finite-element methods in semiconductor device simulation,” *IEEE Transactions on Electron Devices*, vol. 24, pp. 1082–1089, August 1977.

LIST OF FIGURES

1	CCD Detector Array	25
2	CMOS Detector Array	26
3	Structure of Thin Film on ASIC (TFA) Photodetector	27
4	Structure of Silicon on Insulator (SOI) Photodetector	28
5	Structure of Flip Chip Photodetector	29
6	Contact-bounded 1D Photodetector Model	30
7	Numerical Solver Flowchart	31
8	A pipeline is generated to obtain results in terms of the variation of one simulation parameter.	32
9	The deviation and the internal electric field associated with the numerical solution.	33
10	For the analytical solution the excess carrier concentration is considered negligible	34
11	The optical generation results from the analytical method do not preserve the continuity condition, which is in contrast to the numerical method.	35
12	The photo-current signal to dark-current background contrast ratio peaks at the $0.1 \mu m$ optimal length.	36
13	The photo-current density calculated using both analytical and numerical methods for varying injection levels	37
14	Tracking shows that the numerical solution converges after only two iterations.	38
15	The photo-current density calculated using both analytical and numerical methods for varying applied voltages	39

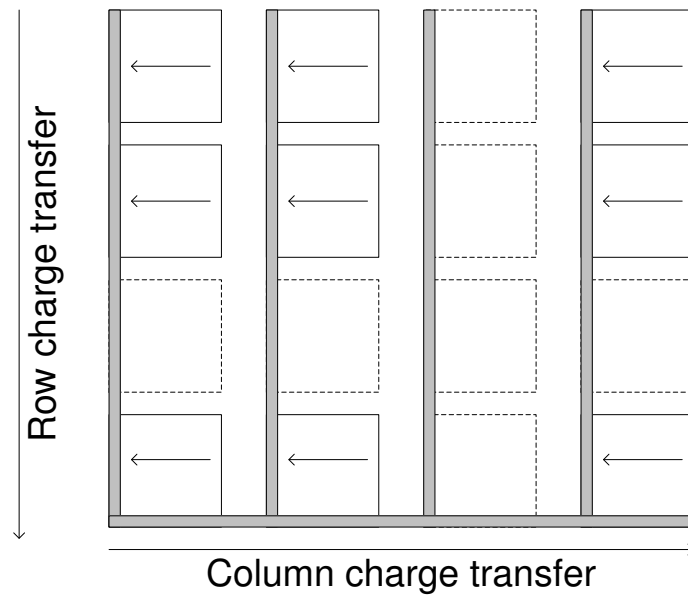


Fig. 1. CCD Detector Array

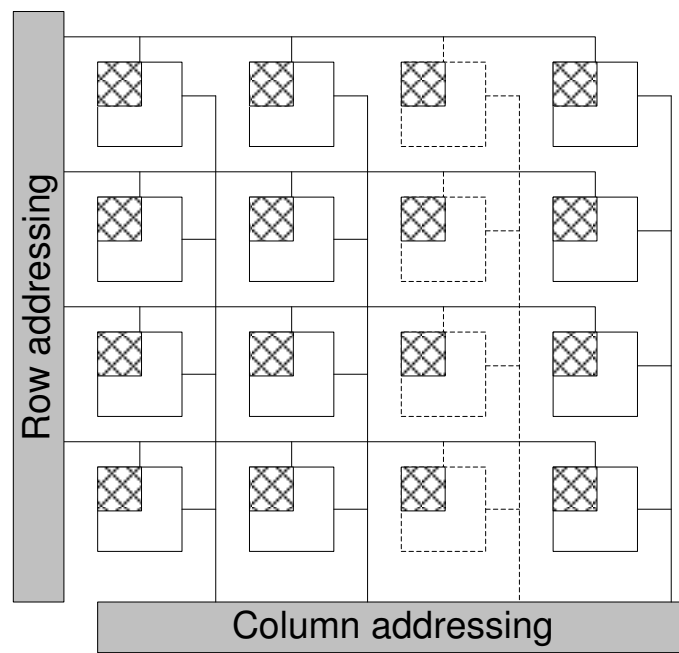


Fig. 2. CMOS Detector Array

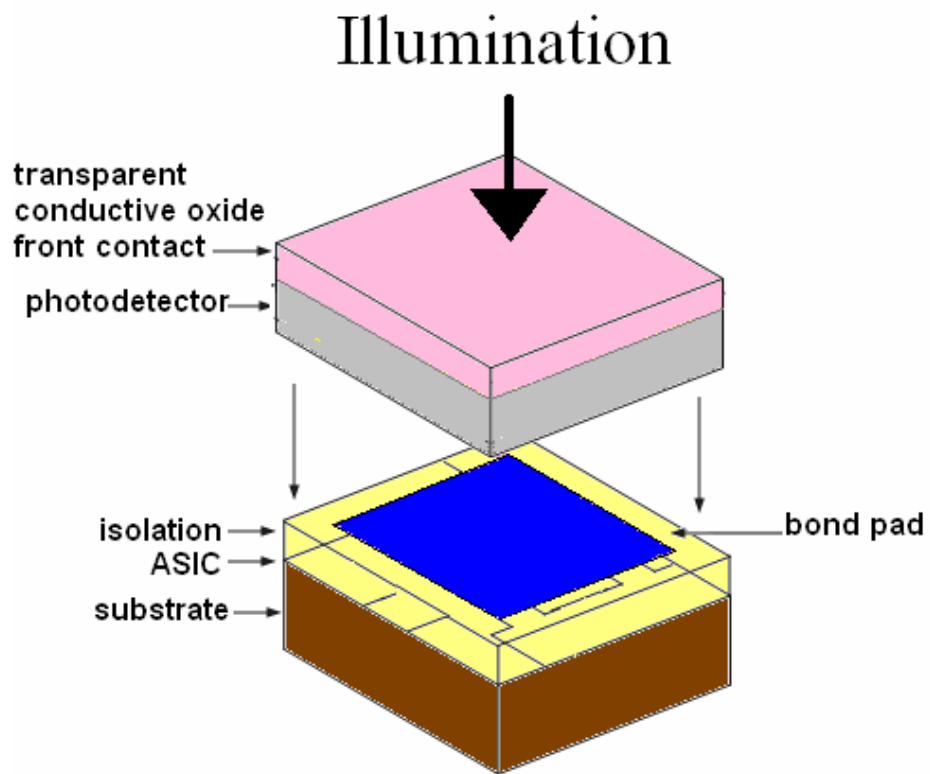


Fig. 3. Structure of Thin Film on ASIC (TFA) Photodetector

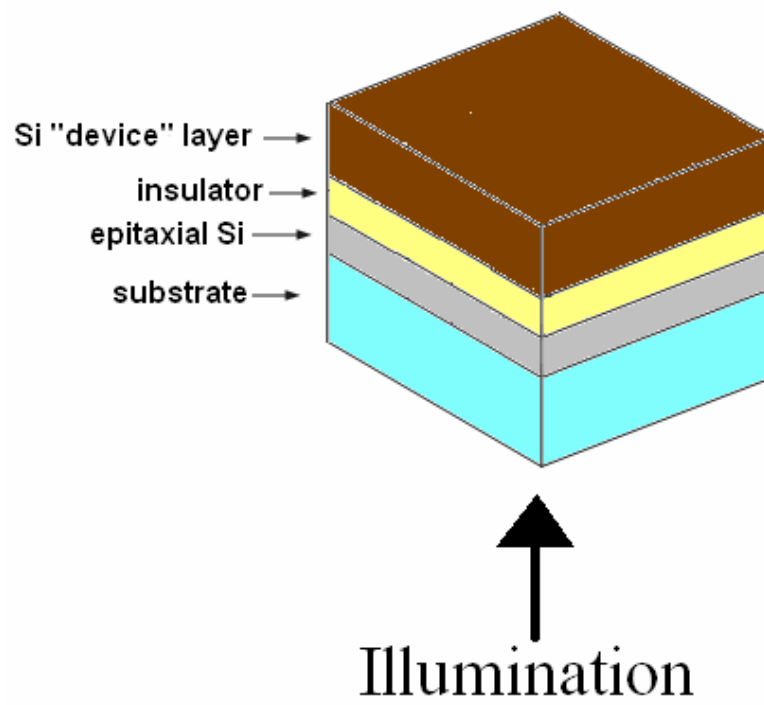


Fig. 4. Structure of Silicon on Insulator (SOI) Photodetector

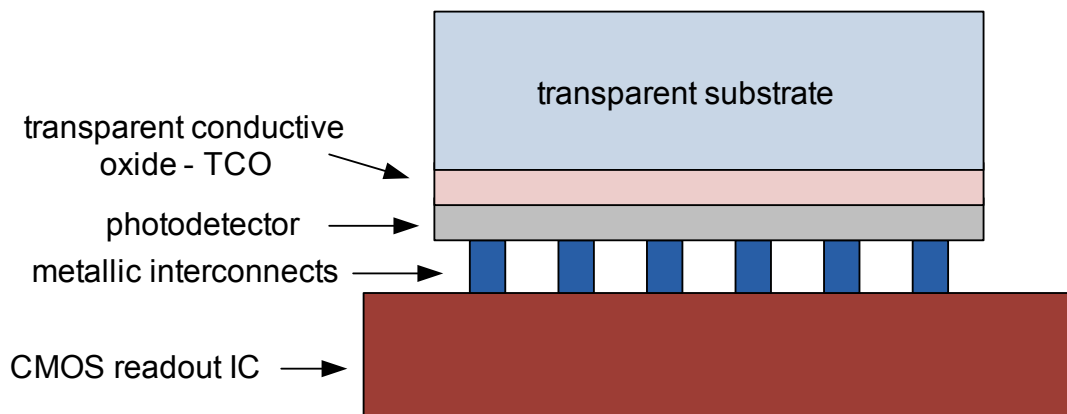


Fig. 5. Structure of Flip Chip Photodetector

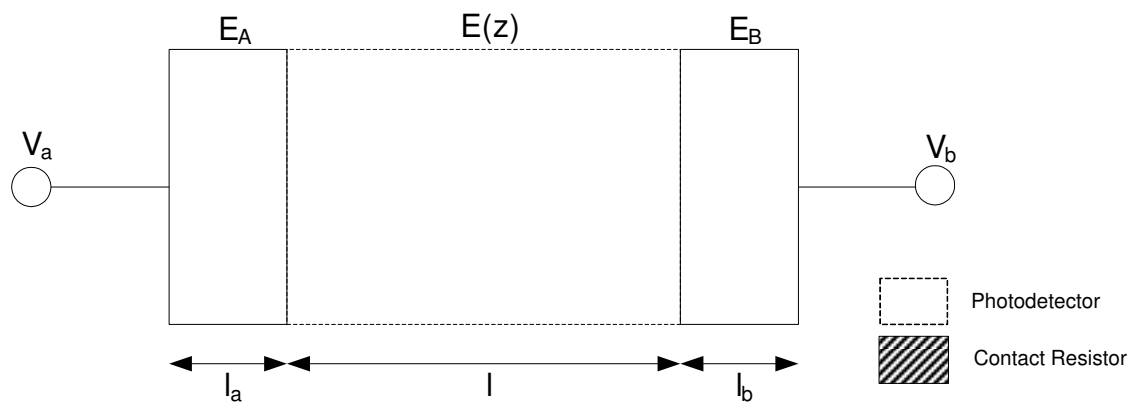


Fig. 6. Contact-bounded 1D Photodetector Model

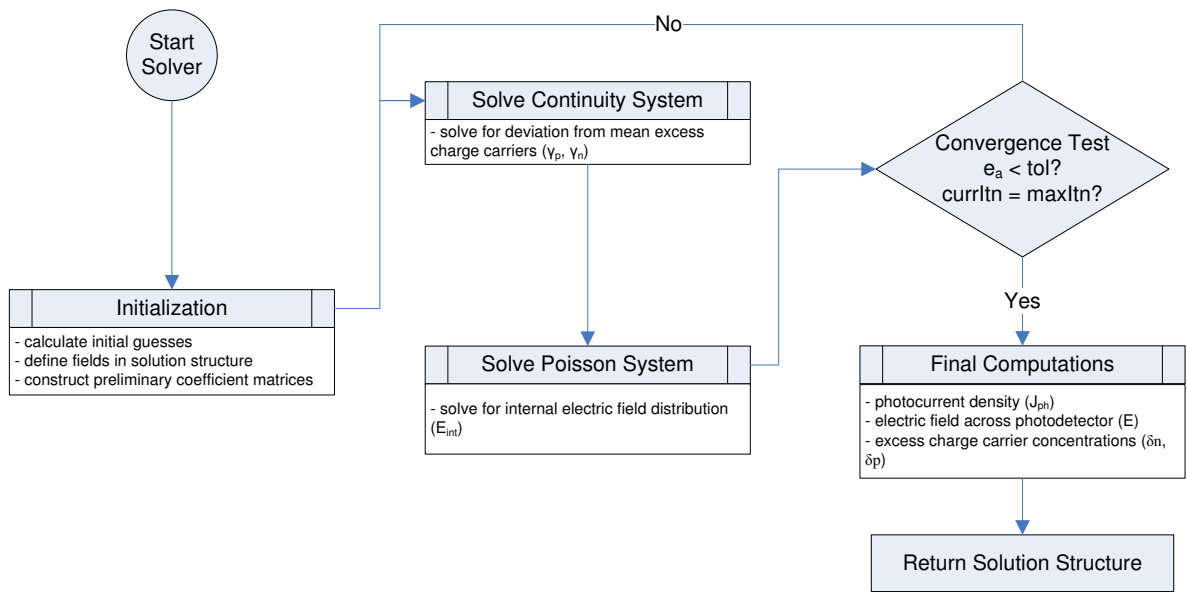


Fig. 7. Numerical Solver Flowchart

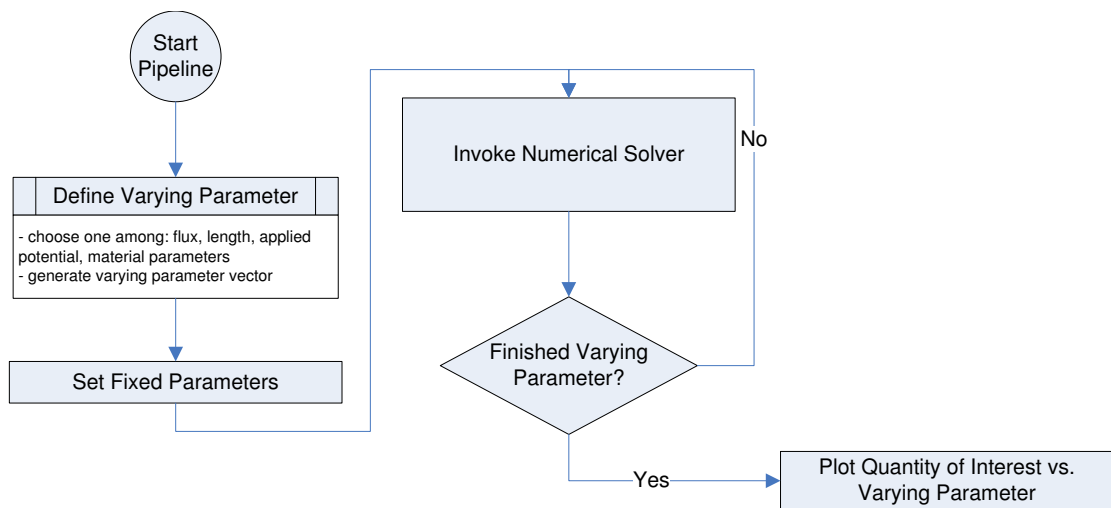


Fig. 8. A pipeline is generated to obtain results in terms of the variation of one simulation parameter.

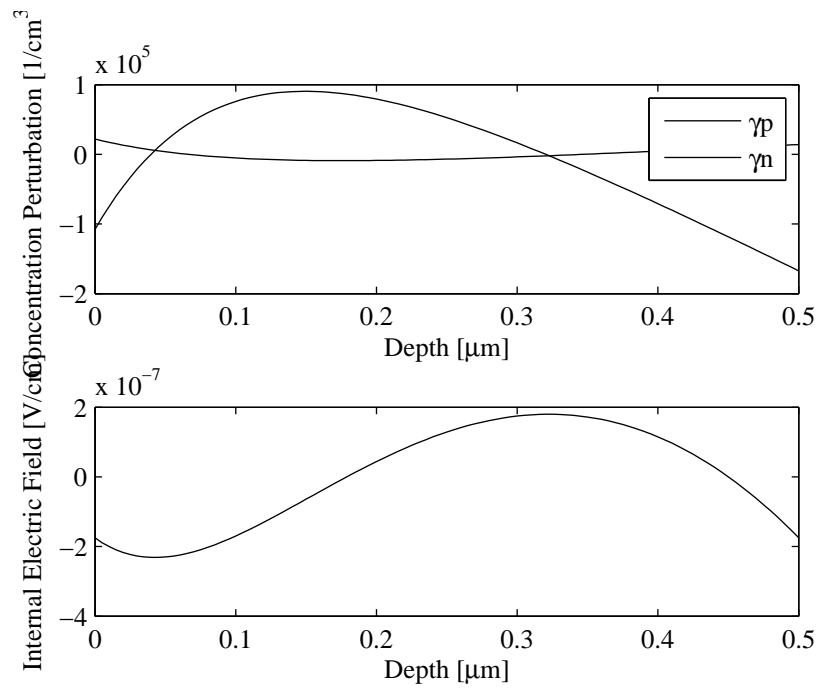


Fig. 9. The deviation and the internal electric field associated with the numerical solution.

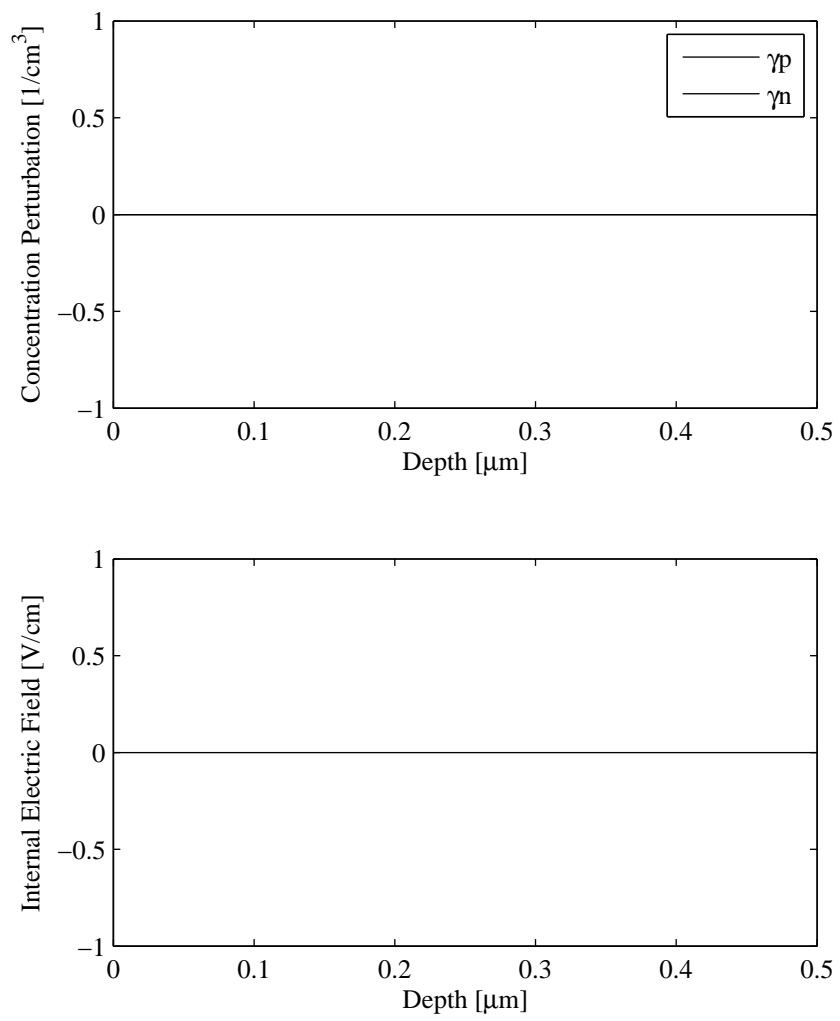


Fig. 10. For the analytical solution the excess carrier concentration is considered negligible

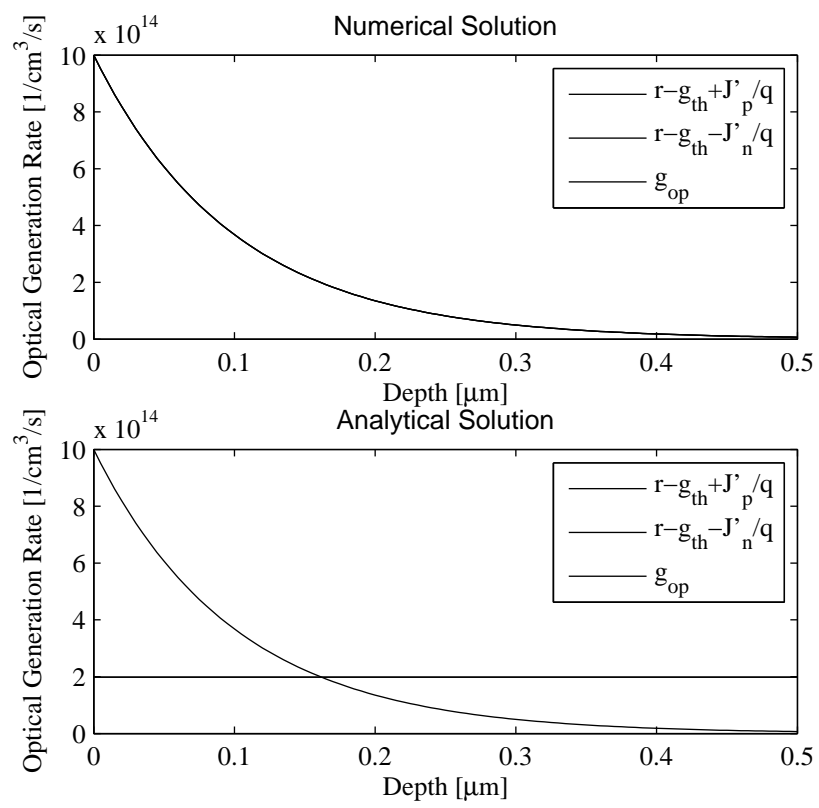


Fig. 11. The optical generation results from the analytical method do not preserve the continuity condition, which is in contrast to the numerical method.

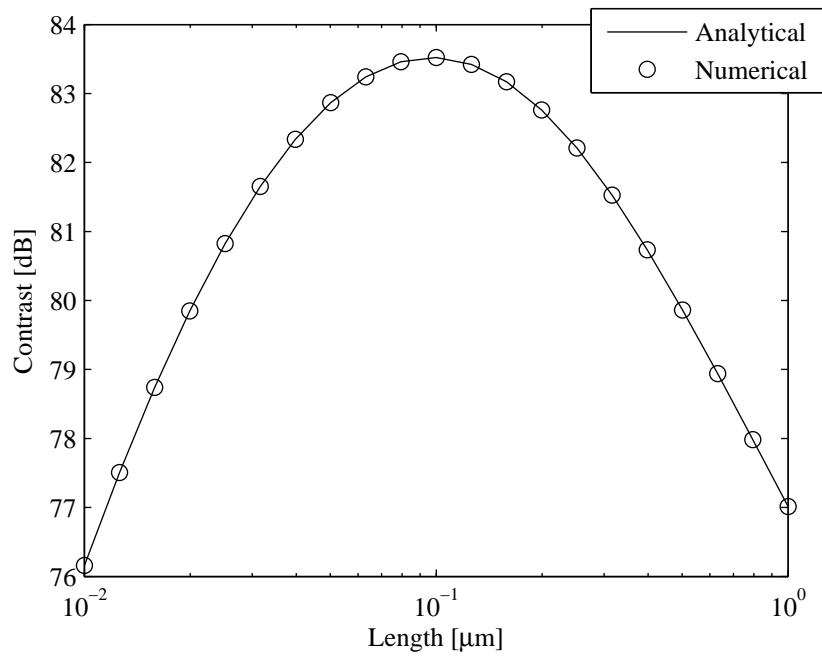


Fig. 12. The photo-current signal to dark-current background contrast ratio peaks at the $0.1 \mu m$ optimal length.

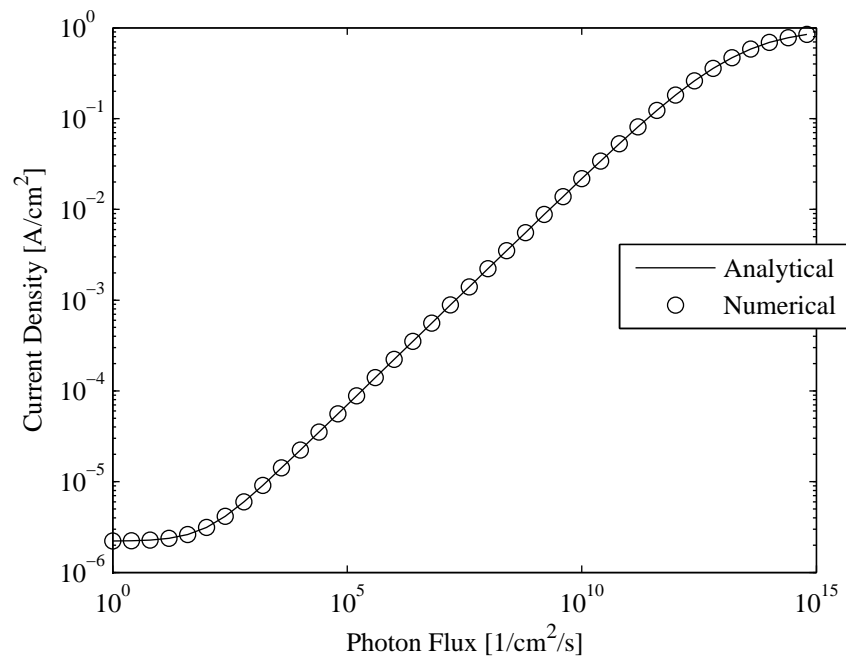


Fig. 13. The photo-current density calculated using both analytical and numerical methods for varying injection levels

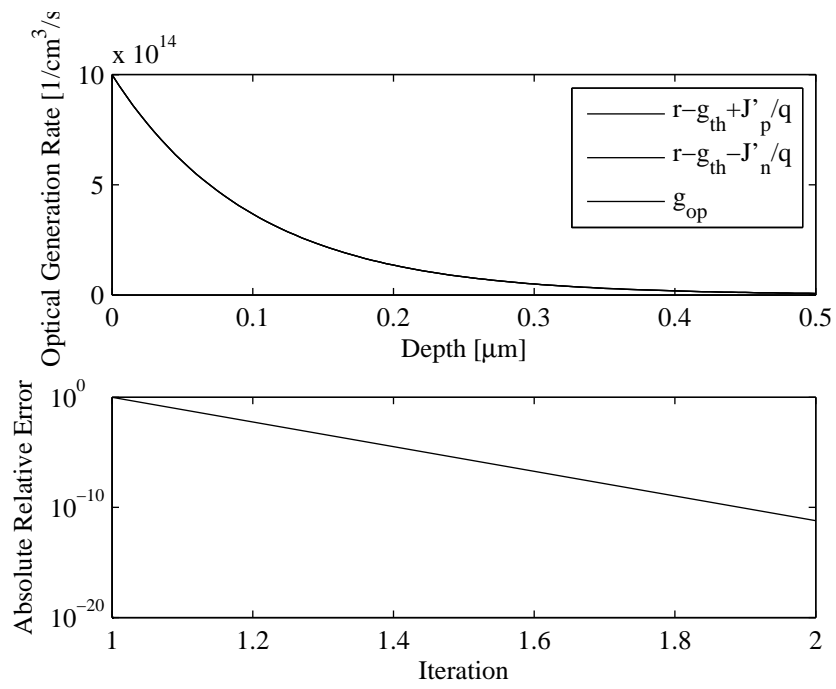


Fig. 14. Tracking shows that the numerical solution converges after only two iterations.

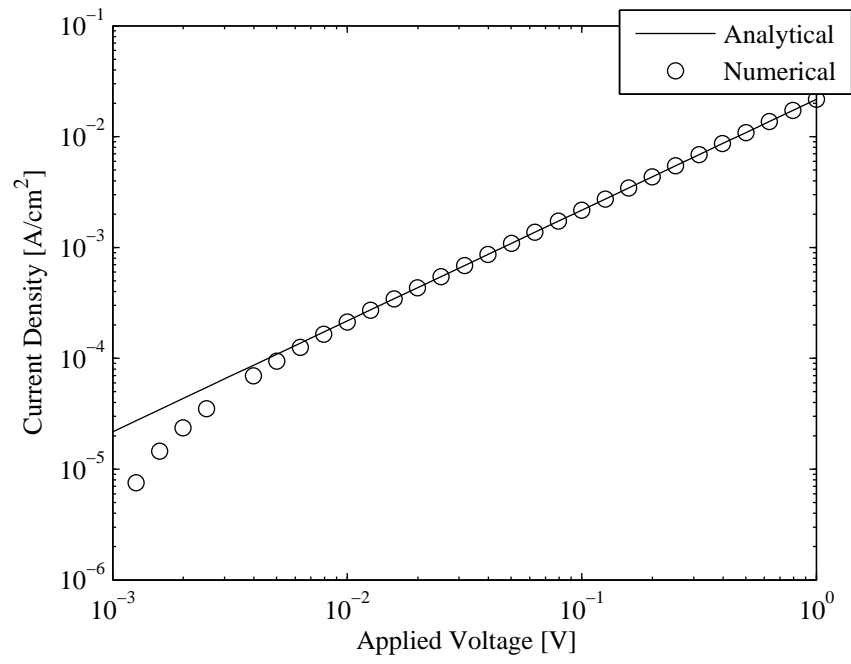


Fig. 15. The photo-current density calculated using both analytical and numerical methods for varying applied voltages